

Circumnuclear Multi-phase Gas in Circinus Galaxy III: Structure of the Nuclear Ionized Gas

KEIICHI WADA,^{1,2,3} KENSUKE YONEKURA,^{1,4} AND TOHRU NAGAO²

¹*Kagoshima University, Graduate School of Science and Engineering, Kagoshima 890-0065, Japan*

²*Ehime University, Research Center for Space and Cosmic Evolution, Matsuyama 790-8577, Japan*

³*Hokkaido University, Faculty of Science, Sapporo 060-0810, Japan*

⁴*NEC Aerospace Systems, Ltd.*

ABSTRACT

We investigate the properties of the ionized gas irradiated by an active galactic nucleus (AGN) based on our “radiation-driven fountain” model for the nearest type-2 Seyfert galaxy, the Circinus galaxy (Wada et al. 2016). We conducted “quasi-three dimensional” spectral analysis using the spectral synthesis code CLOUDY and obtained the surface brightness distributions of lines, such as H α , H β , [OIII], [NII], and [SII] for the central 16-parsec region. The ionized regions observed based on these lines show a conical morphology around the rotation axis, even if we do not phenomenologically postulate the presence of an optically thick “torus”. This region also shows non-uniform internal structures, reflecting the inhomogeneous structure of fountain flows. Using ionization diagnostic diagrams, we investigated the spectral properties of the ionized gas. The diagrams based on the line ratios of [NII]/H α and [SII]/H α show that most regions of the cone have the same properties as those in the narrow line regions (NLRs) in AGNs, whereas using [OI]/H α , the central 10-pc regions are rather LINER-like. The gas density, temperature, and ionizing parameter in regions identified as “NLR” are typically $n \sim 300 - 1500 \text{ cm}^{-3}$, $T \sim 1 - 3 \times 10^4 \text{ K}$, and $U \sim 0.01$, respectively. The morphology and [OIII] intensity are similar to the base of the observed [OIII] cone in the Circinus galaxy, implying some physical connections with the origin of the ~ 100 parsec scale NLR.

Keywords: galaxies: active – galaxies: nuclei – galaxies: ISM – radiative transfer

1. INTRODUCTION

In the standard picture of active galactic nuclei (AGNs), an AGN hypothetically consists of an accretion disk around a supermassive black hole, a broad emission line region, a dusty “torus”, and a narrow emission line region (NLR). NLRs are spectroscopically characterized by narrow (several 100 km s^{-1}) emis-

sion lines, and they spatially extend from tens of parsecs to a few kiloparsecs from the nucleus. Therefore, these regions can be spatially resolved in nearby AGNs, which are characterized by conical structures with clumpy internal morphologies (e.g. Marconi et al. 1994; Schmitt & Kinney 1996; Veilleux et al. 2001; Sharp & Bland-Hawthorn 2010; Müller-Sánchez et al. 2011). It has been determined that NLRs are gases photo-ionized by a power-law spectrum from the nucleus (Davidson & Netzer 1979; Evans & Dopita 1986; Binette et al. 1996; Ko-

mossa & Schulz 1997; Nagao et al. 2006), showing characteristic lines, such as $H\alpha$, $H\beta$, $[OIII] \lambda 5007$, $[NII] \lambda 6583$, and $[SII] \lambda\lambda 6716, 6731$ ¹.

The structures of the ISM in NLRs on the parsec scale are still not resolved, even in nearby AGNs. Various theoretical models of the emitting gas have been proposed, in which the ISM is assumed to consist of single- or multi-component clouds illuminated by nuclear radiation (Baldwin et al. 1995; Ferguson et al. 1997; Murayama & Taniguchi 1998; Nagao et al. 2003; Groves et al. 2004, e.g.) (See also a review by Groves (2007)). Imaging observations and long-slit spectra acquired by the Hubble Space Telescope/WFPC2 and STIS have been used to study the fundamental three-dimensional geometry and conditions of the NLR gases in some nearby AGNs, such as NGC 1068, NGC 4151, Mrk 3, and Mrk 573 (e.g. Kraemer & Crenshaw 2000; Crenshaw et al. 2000; Das et al. 2005, 2006, 2007; Fischer et al. 2010; Crenshaw et al. 2010). These studies suggest that the gases in NLRs form intrinsically biconical outflows consisting of multiple components, whose conditions are determined by the central radiation propagating through the media around AGNs.

However, the origin of such outflowing, multi-component gas is not clear, and the reason why the conical and clumpy morphology of NLRs is formed is still an open question. The conical shape suggests that the radiation from the central source is spatially limited by the optically thick “torus”, that the distribution of the outflowing gas is intrinsically conical, or both.

Instead of assuming phenomenological models, in which the geometry and properties of the “torus” and outflowing gas are postulated, here

we use a physics-motivated, three-dimensional hydrodynamic model. Recently, we proposed a novel, dynamic picture of the ISM in the central tens of parsecs of AGNs, based on three-dimensional radiation-hydrodynamic calculations, i.e., a radiation-driven fountain (Wada 2012). In this picture, the outflowing, multi-phase gas with dust is naturally formed, and we found that it is not necessary to postulate a donut-like “torus” to explain type-1 and -2 dichotomies in the spectral energy distribution (SED) (Schartmann et al. 2014).

In this paper, we focus on the spectral properties of the fountain flows illuminated by the AGN, to determine whether they show the properties of the observed NLRs. One should note that our current hydrodynamic model is still spatially limited, i.e. $r \leq 16$ pc, therefore it may not be used to explain the general morphology of NLRs extended to several hundred parsecs; however, it can be compared with the central part of the NLR in the nearest ($D = 4.2$ Mpc, Tully et al. (2009)) type-2 Seyfert galaxy, the Circinus galaxy.

The structure of this paper is as follows. In §2, we briefly describe the input hydrodynamic model, i.e., the radiation-driven fountain (Wada et al. 2016), and the model set-up for *quasi-multi-dimensional* CLOUDY simulations. Numerical results are shown in §3, and their implications are discussed with respect to the observed NLR in §4. A summary is given in §5.

2. CLOUDY SIMULATIONS BASED ON THE HYDRODYNAMIC MODEL

2.1. Input model: Radiation-driven fountain

Wada (2012) proposed that the obscuring structures around AGNs, in which outflowing and inflowing gases are driven by radiation from the accretion disk, form a geometrically thick disk-like structure on the scale of a few parsecs to tens of parsecs. The quasi-steady “poloidal” circulation of gas, i.e., the

¹ Shock excitation should be also considered to explain some lines, such as $[FeII]$ and $[PII]$, that form NLRs in some Seyfert galaxies (Mouri et al. 2000; Oliva et al. 2001; Storchi-Bergmann et al. 2009; Terao et al. 2016). See also Kraemer & Crenshaw (2000) for modeling the origin of emission lines in NGC 1068.

“radiation-driven fountain,” may obscure the central source (Wada 2015). The differences in SEDs of typical type-1 and -2 Seyfert galaxies are reasonably explained by changing the viewing angle without assuming a donut-like optically thick torus (Schartmann et al. 2014). Wada et al. (2016) applied this radiation-driven fountain model with an X-ray-dominated region chemistry to the central 16-pc region of the Circinus galaxy. They found that dense molecular gases ($n_{\text{H}_2} \gtrsim 10^3 \text{ cm}^{-3}$) are mostly concentrated around the equatorial plane, and atomic gas (e.g., H^0 and C^0) extends with a larger scale height. There is also “polar” emission in the mid-infrared band ($12 \mu\text{m}$), which is associated with bipolar outflows, as suggested in recent interferometric observations of nearby AGNs (Hönig et al. 2013; Tristram et al. 2014). The viewing angle θ_v toward the nucleus should be larger than 75° (i.e., close to edge-on) to explain the observed SED and $10 \mu\text{m}$ absorption feature of the Circinus galaxy (Prieto et al. 2010).

This best-fit model for the Circinus galaxy was used in Wada et al. (2018), and the results explain the structures of the cold molecular gas located on the outskirts of the bright infrared region. These results were derived from 3-D non-local thermodynamic equilibrium line transfer calculations for ^{12}CO lines. These results are consistent with various aspects of ALMA Cycle-4 observations, as discussed in Izumi et al. (2018).

In this paper, we focus on a cone structure occupied by an inhomogeneous, diffuse, ionized gas in this fountain model (Wada et al. 2016). The outflows surrounded by geometrically thick atomic/molecular gas could be the origin of the NLRs. To observe the spectral properties of the outflowing gas in the numerical model, we apply a spectral synthesis code, CLOUDY (Ferland et al. 2017), to the same snapshot data used in Wada et al. (2018).

2.2. Radiative transfer using CLOUDY

As shown in Fig. 1, one eighth of the 3-D grid data (i.e., density and temperature) from the 256^3 Cartesian grid cells in the radiation-hydrodynamic simulation (Wada et al. 2018) is reformed to uniformly spaced polar grid cells with $(N_r, N_\theta, N_\phi) = (16, 16, 16)^2$. The radial size of each grid cell is 1 parsec.

We then ran the spectral synthesis code CLOUDY (version 17.02) (Ferland et al. 2017) for polar grid cells along the *radial direction* from the central source to the outer boundary at $r = 16 \text{ pc}$ (Fig. 1a). Therefore, CLOUDY is called 16^3 times to obtain the intensity distributions of the emission lines. Note that the present calculation is *not fully* three-dimensional, in the sense that non-radial photons that emerge from other grid cells are not taken into account as the incident radiation for a CLOUDY call.

The SED of the central source is given using CLOUDY’s AGN command, which assumes the spectral:

$$f_\nu = \nu^{\alpha_{uv}} \exp(-h\nu/kT_{BB}) \exp(-kT_{IR}/h\nu) + a\nu^{\alpha_x},$$

where $\alpha_{uv} = -0.5$, $T_{BB} = 10^5 \text{ K}$, $\alpha_x = -1$, a is a constant that yields $\alpha_{ox} = -1.4$, and $kT_{IR} = 0.01 \text{ Ryd}$. The bolometric luminosity of the central source is $L_{bol} = 5 \times 10^{43} \text{ erg s}^{-1}$, and the flux changes depending on direction as $\cos\theta$ (θ is the angle from the z-axis), as we assume that the UV radiation is dominated by the thin accretion disk. We assume solar metallicity. The filling factor is set to unity. One should note that the choice of the filling factor of unity does not mean that the outflowing gas is “uniform”. The radiation-driven fountain flows are not uniform on the scale of several

² The three-dimensional density field of the radiation-driven fountain is not perfectly axisymmetric and is not symmetric in the equatorial plane, but we think that 1/8 of the total box (i.e., the volume in $x > 0$, $y > 0$, and $z > 0$) is enough to study the emission line properties in fountain flows

parsecs. However, we here do not assume unresolved clumpy internal structures in one grid cell for each CLOUDY calculation. For simplicity, we intend to assume the least number of free parameters.

The transmitted SED, calculated with CLOUDY, is used as an incident SED for the next outward radial cell, and this procedure is repeated up to the outer edge (i.e., $r = 16$ pc) for a given radial ray. The line intensities, such as those of $H\alpha$, $H\beta$, $[OIII] \lambda 5007$, $[OI] \lambda 6300$, $[NII] \lambda 6583$, and $[SII] \lambda \lambda 6716, 6731$, are collected using the “save line list” command and are integrated along the line-of-sight (y -direction) to obtain surface brightness maps.

3. RESULTS

3.1. Intensity distributions

Figure 2 shows the surface brightness distributions of the $[OIII] \lambda 5007$ and $H\beta$ lines. Both distributions show a conical shape around the rotation axis (i.e., z -axis). The half opening angle of the $[OIII]$ emission is approximately 45 degrees. Note that this morphology is not caused by an optically thick “torus”, but it is rather a natural consequence of non-spherical radiation emitted from the central accretion disk and the resulting funnel-like fountain flows (Fig. 1b). Radiation from a thin accretion disk and obscuration of the surrounding material causes ionization photons to escape into the funnel-like structures (see Fig. 1b,c and Wada (2012)). In a three-dimensional view, the $[OIII]$ bright regions are distributed mostly at the inner wall of the funnel flow (i.e., the yellow regions shown in Fig. 1b), and this is also suggested from observations of near-by AGNs (e.g. Das et al. 2006; Fischer et al. 2010; Crenshaw et al. 2010; Müller-Sánchez et al. 2011).

It is also notable that the internal structures of $[OIII]$ and $H\beta$ are not uniform on the scale of several parsecs, reflecting the inhomogeneous structures of the outflowing gas, which varies

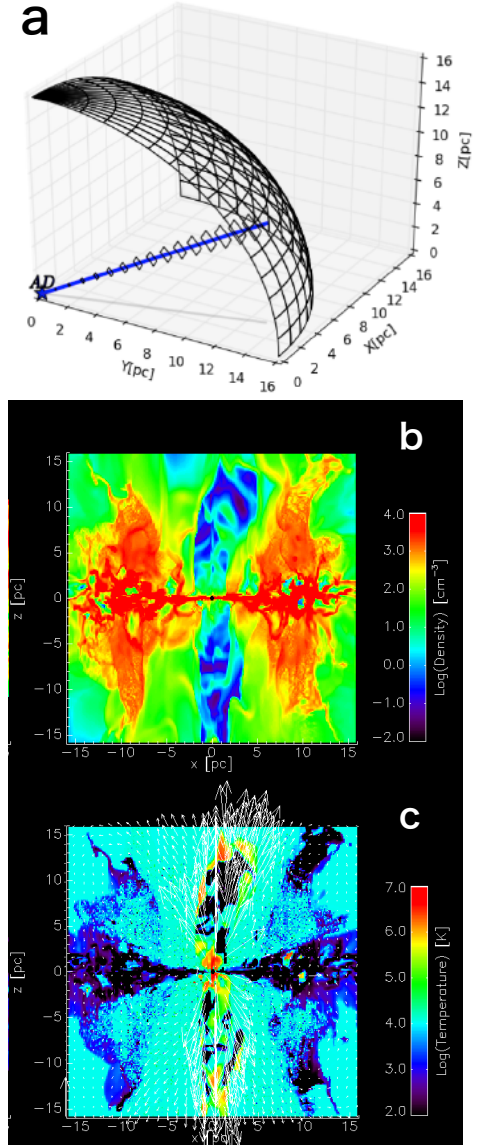


Figure 1. a) Configuration of the calculation. Radiation from the central accretion disk (denoted as AD) is calculated by calling CLOUDY along a radial ray. (b) Three-dimensional density and (c) temperature grid data in the $y = 0$ plane is taken from a radiation-hydro simulation (Wada et al. 2016). The rotation axis of the circumnuclear disk is along the z -axis.

by an order of magnitude in the column density for a given line-of-sight in the radiation-driven fountain (Wada 2015; Wada et al. 2016). Propagating the ionizing photon through the non-uniform media also causes variation of the spec-

tral properties along rays (see also Fig. 5 and related discussion). The [OIII] and $H\beta$ bright regions roughly coincide, but as Fig. 2c shows, the [OIII] is relatively brighter with respect to the $H\beta$ at the outer part ($r \gtrsim 10$ pc) in the ionizing cone.

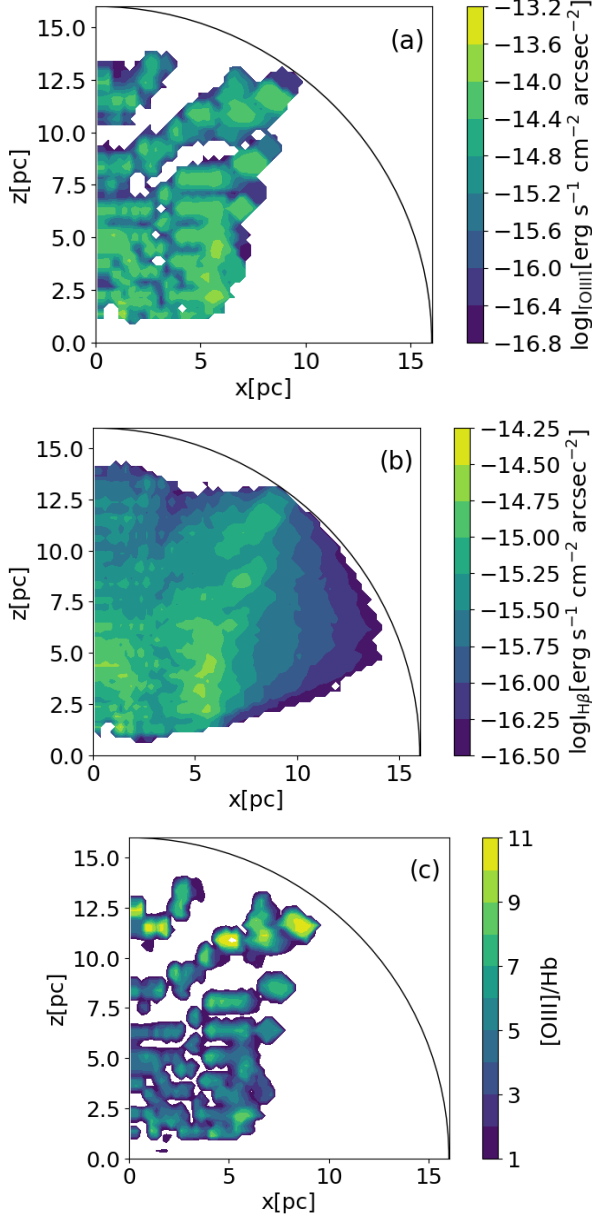


Figure 2. a) [OIII] surface brightness distribution. The rotational axis points along the z -axis. b) Same as a), but for $H\beta$. c) Distribution of [OIII]/ $H\beta$ line ratio.

3.2. Ionization diagnostic diagrams

The ionization diagnostic diagrams, or so-called BPT diagrams (Baldwin et al. 1981; Veilleux & Osterbrock 1987), use two pairs of line ratios to distinguish the properties of emission lines in the narrow-line regions (NLRs) of Seyfert galaxies, low ionization nuclear emission-line regions (LINERs), and starburst galaxies. Here, we apply ionization diagnostic diagram criteria based on Kewley et al. (2001) to the [OIII] $\lambda 5007$, [NII] $\lambda 6583$, [SII] $\lambda\lambda 6717, 30$, $H\alpha$, and $H\beta$ intensities obtained by the calculations described in §3.1.

Three pairs of line ratios are plotted in Fig. 3a-c. Note that each point represents the emission line ratios for a given position in the observer’s plane, not for *one galaxy*, as in the usual BPT diagrams. These plots can be used to diagnose the *local* properties of the photo-ionized regions in circumnuclear ISM on scales of a few parsecs. In observations, similar plots have been obtained in some nearby galaxies with galactic winds using an integral-field spectrograph (IFU) (Sharp & Bland-Hawthorn 2010) (see their Fig. 21 for the Circinus galaxy), however, their spatial resolutions are still too large to make direct comparison with the present model (see also Fig. 7).

As the [OIII] flux weighted average (black filled circle) shows, the BPT diagrams based on [SII]/ $H\alpha$ (Fig. 3a) and [NII]/ $H\alpha$ (Fig. 3b) suggest that the ionizing cone in our model can be diagnosed as “NLR”s or “AGN”. However, Fig. 3c shows that even the [OIII] bright regions are located in part in the “LINER” domain (see discussion below).

Figures 4a-c show the distributions of the three emission line regions diagnosed from Figs. 3a-c, respectively. Relatively bright [OIII] regions (i.e. $> 10^{-15} \text{ erg s}^{-1} \text{cm}^{-2} \text{arcsec}^{-2}$) are plotted. In Figs. 4a and 4b, it is notable that the “NLR” grids (blue grids) dominate the outflow regions around the z -axis and form a

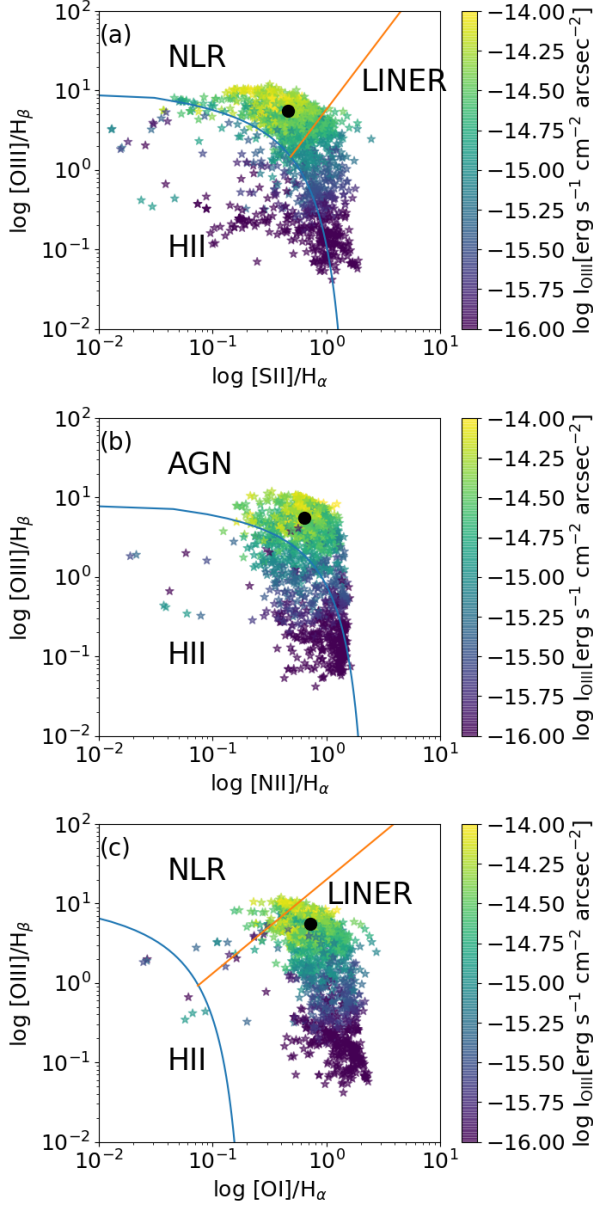


Figure 3. Ionization diagnostic diagrams for three emission line pairs. The solid blue curves show the starburst limit, and the orange lines show the limit between NLRs and LINERS (Kewley et al. (2001)). Color represents the [OIII] surface brightness. The black filled circles show the [OIII] brightness weighted averages.

conical shape. The small patches of “HII” (red grids) are caused by the grids with relatively less brightness in [OIII] in the BPT diagram (Fig. 3a-b). Note that this does not mean that the ionized regions in the present model are caused

by photons from star-forming regions. In fact, we here assume only the AGN as the ionizing source, but the incident SEDs may significantly change when the radiation radially propagates through the gas around the AGNs as discussed below.

In contrast to Fig. 4a and 4b, the [OI] -based diagram (Fig. 4c) shows that the region at $r \lesssim 10$ pc is mostly categorized as “LINER”, reflecting the distribution in the line-diagnostic diagram (Fig. 3c), although some regions identified as “NLR” are located at $r \gtrsim 10$ pc, where [OIII]/H β is relatively large (see Fig. 2c). This result is seemingly paradoxical because the Circinus galaxy is not apparently LINER. This can be understood by the fact that [OI] becomes relatively stronger relative to other lines, if UV emission is dominated by X-ray emission in the incident SEDs (Nagao et al. 2002). In fact, Fig. 5 shows that the SEDs are heavily attenuated along a ray from the central source, especially in the UV range. This “filtered” radiation may change the physical conditions and line emissions of the ionized gas, depending on the column density, as pointed out for Markarian 3 (Collins et al. 2009).

3.3. Physical properties of the gas in NLRs

The physical conditions of the ISM in NLRs have been inferred from spectroscopic data in nearby AGNs. For example, from the line ratio of [SII] $\lambda\lambda 6716, 6731$, the electron density is estimated to be $n \simeq 2000 \text{ cm}^{-3}$ (Koski 1978). More recently, Zhang et al. (2013) presented a statistical study based on 15,000 objects in SDSS DR7 and found that typical density and temperature ranges for the NLR gas are $n \simeq 100 - 10^4 \text{ cm}^{-3}$ and $T_e \simeq 1 - 2 \times 10^4 \text{ K}$, respectively. The origin of these line emitting gases could be AGN-driven outflows. In the previous section, we found that emission lines from the outflow show characteristic properties of NLRs. The gas density, temperature, and ionizing parameter in the “NLR” domains are plotted in Fig. 6. Local

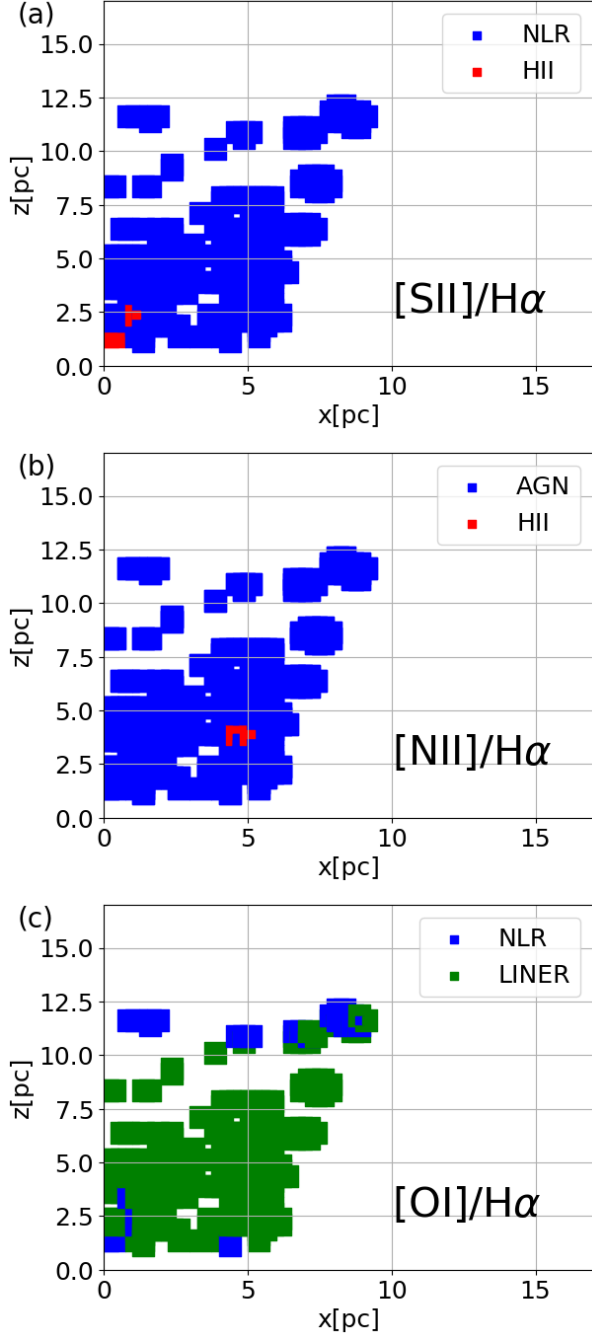


Figure 4. a) Distribution of the three emission line regions using the $[\text{SII}]/\text{H}\alpha$ - $[\text{OIII}]/\text{H}\beta$ diagram (Fig. 3a). b) Same as Fig.4a, but based on $[\text{NII}]/\text{H}\alpha$ - $[\text{OIII}]/\text{H}\beta$ (Fig. 3b), and c) $[\text{OI}]/\text{H}\alpha$ - $[\text{OIII}]/\text{H}\beta$ (Fig. 3c). Only $[\text{OIII}]$ bright regions with $> 10^{-15} \text{ erg s}^{-1} \text{ cm}^{-2} \text{ arcsec}^{-2}$ are shown.

density and temperature are taken from the input hydrodynamic model (i.e., 4096 grid cells). The ionization parameter U , which is the ratio

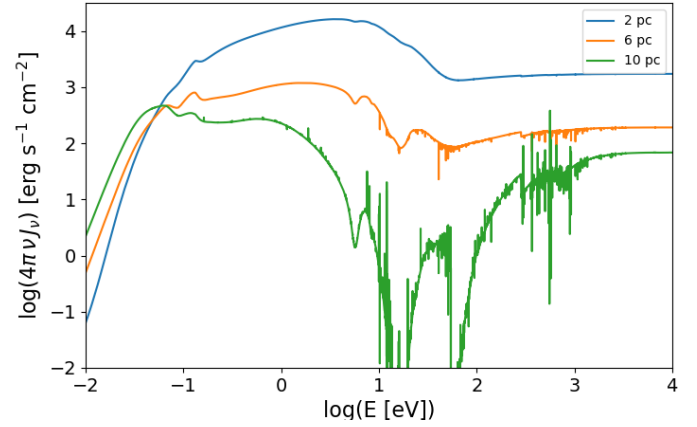


Figure 5. Radial change of SEDs at $r = 2, 6$, and 10 pc from the center along a ray of $\theta = 40^\circ$ from the rotational axis.

of the ionizing photon density to the electron density, is defined as

$$U \equiv \frac{1}{4\pi r^2 c n_{\text{H}}} \int_{\nu_0}^{\infty} \frac{L_{\nu}}{h\nu} d\nu. \quad (1)$$

Here, U is taken from each CLOUDY output. The grid cells are counted where the $[\text{OIII}]$ local intensity is brighter than 0.3% of its maximum value. We found that the gas density in NLR is approximately $n \sim 300 - 1500 \text{ cm}^{-3}$, The temperature is $T \sim 1 - 3 \times 10^4 \text{ K}$, and $U \sim 0.01$. These “NLR” gases are located mostly at the *inner* surface of the bicone (yellow regions in Fig 1b), as suggested by observations of NLRs in nearby AGNs (e.g. Das et al. 2006; Müller-Sánchez et al. 2011), although our model here may be applied only to the innermost region of NLRs, extended to $\sim 100 \text{ pc}$ (see also the discussion in §4.1).

4. DISCUSSION

4.1. Comparison with observations

In Fig. 7, our $[\text{OIII}]$ map (Fig. 2a) is compared with the one obtained by the Integral Field Unit observation using the Anglo-Australian Telescope (Sharp & Bland-Hawthorn 2010) and the Hubble Space Telescope/WFPC2 (Wilson et al. 2000). A CO(3-2) map obtained by ALMA

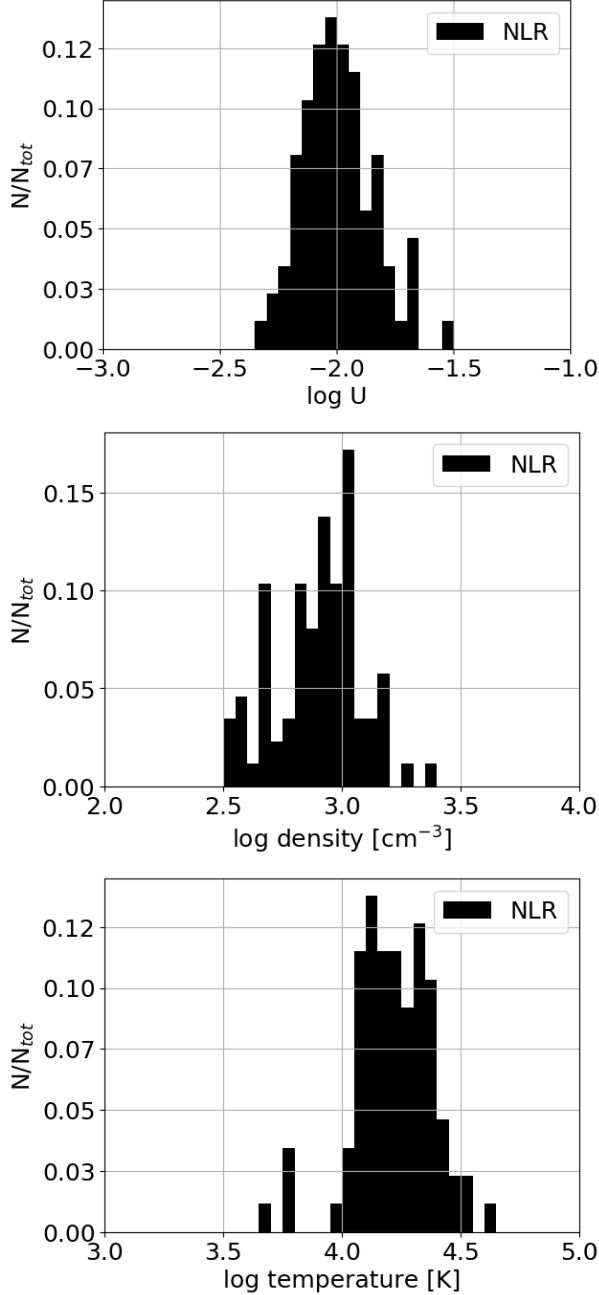


Figure 6. Histograms of the ionizing parameter U , density, and temperature in grid cells categorized as NLR using $[\text{SII}]/\text{H}\alpha$ and $[\text{OIII}]/\text{H}\beta$.

(Izumi et al. 2018) is also shown to elucidate the multi-phase structures in the central region of Circinus. The IFU observations by Sharp & Bland-Hawthorn (2010) show a conical ionizing region extending to $r \sim 400 - 500$ pc by observing $[\text{OIII}]$, $\text{H}\alpha$, $\text{H}\beta$, $[\text{NII}]$, and $[\text{SII}]$ lines (see

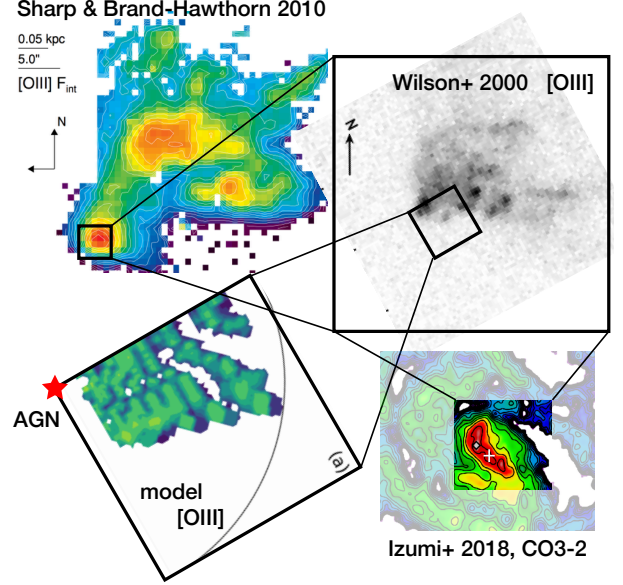


Figure 7. Comparison of Fig. 2a with observed $[\text{OIII}]$ (Wilson et al. 2000; Sharp & Bland-Hawthorn 2010) and $\text{CO}(3-2)$ (Izumi et al. 2018) in the Circinus galaxy.

their Figs. 19 and 20). Their observed resolution was 0.7 arcsec ($= 14.3$ pc), which is ten times larger than our model. The innermost region of the observed ionizing cone (< 50 pc) is mostly categorized as “NLR” in their ionization diagnostic diagram, but direct comparison with Fig. 4 is not relevant. Wilson et al. (2000) presented images of $[\text{OIII}] \lambda 5007$ and $\text{H}\alpha$ with 0.046 arcsec (0.9 pc) angular resolution in the central 20-pc region of the Circinus galaxy using the Hubble Space Telescope/WFPC2. The observed $[\text{OIII}]$ ionizing cone (< 20 pc) has clumpy internal structures, and this is also the case in our model. The surface brightness of the brightest spots in the $[\text{OIII}]$ cone are approximately $10^{-16} \text{ erg s}^{-1} \text{ cm}^{-2} \text{ pixel}^{-1} \sim 10^{-14} \text{ erg s}^{-1} \text{ cm}^{-2} \text{ arcsec}^{-2}$, which is comparable with that shown in Fig. 2a.

The origin of the knot-like structures of the NLR seen in Sharp & Bland-Hawthorn (2010) is still an open question. Its morphology shows some self-similarity to the innermost structures seen in Wilson et al. (2000) and also in our sim-

ulations. Our model presented here cannot follow the evolution of the AGN-driven outflows on such a large scale. Still, one should note that the outflows driven by AGNs can be intrinsically non-uniform and non-steady; therefore, it would be natural to see the knot-like structures in the emission lines. The radiative transfer effect (e.g., Fig. 5) and time variation of the AGN activity itself could also enhance the non-uniform nature in the emission lines. It is also notable that the physical conditions of the “NLR” gases in our model (§3.3) are consistent with those that have been inferred for the observed narrow line regions.

4.2. Multi-phase nature in the central region

Recently, mid-infrared (MIR) interferometric observations showed that the bulk of the MIR emission comes from dust in the polar region, rather than from the dusty “torus” (Tristram et al. 2014; Asmus et al. 2016). The polar infrared emission is naturally predicted from our radiation-fountain picture (Schartmann et al. 2014). The present results suggest that the fountain flows can be a source of MIR polar emission and line emission from NLRs. Both the ionizing cone presented here and the MIR polar emission extend perpendicular to the molecu-

lar “disk” observed by CO (3-2) using ALMA (Wada et al. 2018; Izumi et al. 2018) (see also Fig. 7). The radiation-driven fountain can naturally explain the multi-phase gas structures around the nucleus, at least for the central region of the Circinus galaxy. Investigating the generality of this picture for other nearby Seyfert galaxies would be an interesting subject for future theoretical and observational studies.

The authors would like to thank the anonymous referee for his/her constructive comments and suggestions. We are grateful to T. Izumi and L. Ho for valuable comments on the manuscript. Calculations were performed with version 17.02 of CLOUDY. We thank G. Ferland and the CLOUDY team for their continuous support. Numerical computations of the radiation-hydrodynamic model were performed on a Cray XC30 at the Center for Computational Astrophysics at the National Astronomical Observatory of Japan. This work was supported by JSPS KAKENHI Grant Numbers 16H03959, 18K18774, 16H01101, and 16H03958. KW thanks Onsala Space Observatory and S. Aalto for their support and hospitality.

REFERENCES

- Asmus, D., Hönig, S. F., & Gandhi, P. 2016, *ApJ*, 822, 109
- Baldwin, J. A., Phillips, M. M., & Terlevich, R. 1981, *PASP*, 93, 5
- Baldwin, J., Ferland, G., Korista, K., & Verner, D. 1995, *ApJL*, 455, L119
- Binette, L., Wilson, A. S., & Storchi-Bergmann, T. 1996, *A&A*, 312, 365
- Collins, N. R., Kraemer, S. B., Crenshaw, D. M., Bruhweiler, F. C., & Meléndez, M. 2009, *ApJ*, 694, 765
- Crenshaw, D. M., Kraemer, S. B., Hutchings, J. B., et al. 2000, *ApJL*, 545, L27
- Crenshaw, D. M., Kraemer, S. B., Schmitt, H. R., et al. 2010, *AJ*, 139, 871
- Davidson, K., & Netzer, H. 1979, *Reviews of Modern Physics*, 51, 715
- Das, V., Crenshaw, D. M., Hutchings, J. B., et al. 2005, *AJ*, 130, 945
- Das, V., Crenshaw, D. M., Kraemer, S. B., & Deo, R. P. 2006, *AJ*, 132, 620
- Das, V., Crenshaw, D. M., & Kraemer, S. B. 2007, *ApJ*, 656, 699
- Evans, I. N., & Dopita, M. A. 1986, *ApJL*, 310, L15
- Ferguson, J. W., Korista, K. T., Baldwin, J. A., & Ferland, G. J. 1997, *ApJ*, 487, 122

- Ferland, G. J. M., Chatzikos, F. Guzman, M. L. Lykins, P. A. M. van Hoof, R. J. R. Williams, N. P. Abel, N. R. Badnell, F. P. Keenan, R. L. Porter, P. C. Stancil
<https://arxiv.org/abs/1705.10877>
- Fischer, T. C., Crenshaw, D. M., Kraemer, S. B., Schmitt, H. R., & Trippe, M. L. 2010, *AJ*, 140, 577
- Groves, B. A., Dopita, M. A., & Sutherland, R. S. 2004, *ApJS*, 153, 75
- Groves, B. 2007, *The Central Engine of Active Galactic Nuclei*, 373, 511
- Hönig, S. F., Kishimoto, M., Tristram, K. R. W., et al. 2013, *ApJ*, 771, 87
- Izumi, T., Wada, K., Fukushige, R., Hamamura, S., Kohno, K., submitted to *ApJ*.
- Kewley, L. J., Dopita, M. A., Sutherland, R. S., Heisler, C. A., & Trevena, J. 2001, *ApJ*, 556, 121
- Komossa, S., & Schulz, H. 1997, *A&A*, 323, 31
- Koski, A. T. 1978, *ApJ*, 223, 56
- Kraemer, S. B., & Crenshaw, D. M. 2000, *ApJ*, 532, 256
- Kraemer, S. B., & Crenshaw, D. M. 2000, *ApJ*, 544, 763
- Marconi, A., Moorwood, A. F. M., Origlia, L., & Oliva, E. 1994, *The Messenger*, 78, 20
- Mouri, H., Kawara, K., & Taniguchi, Y. 2000, *ApJ*, 528, 186
- Müller-Sánchez, F., Prieto, M. A., Hicks, E. K. S., et al. 2011, *ApJ*, 739, 69
- Murayama, T., & Taniguchi, Y. 1998, *ApJL*, 497, L9
- Nagao, T., Murayama, T., Shioya, Y., & Taniguchi, Y. 2002, *ApJ*, 567, 73
- Nagao, T., Murayama, T., Shioya, Y., & Taniguchi, Y. 2003, *AJ*, 126, 1167
- Nagao, T., Maiolino, R., & Marconi, A. 2006, *A&A*, 447, 863
- Oliva, E., Marconi, A., Maiolino, R., et al. 2001, *A&A*, 369, L5
- Prieto, M. A., Reunanen, J., Tristram, K. R. W., et al. 2010, *MNRAS*, 402, 724
- Sharp, R. G., & Bland-Hawthorn, J. 2010, *ApJ*, 711, 818
- Schartmann, M., Wada, K., Prieto, M. A., Burkert, A., & Tristram, K. R. W. 2014, *MNRAS*, 445, 3878 (Sch14)
- Schmitt, H. R., & Kinney, A. L. 1996, *ApJ*, 463, 498
- Storchi-Bergmann, T., McGregor, P. J., Riffel, R. A., et al. 2009, *MNRAS*, 394, 1148
- Terao, K., Nagao, T., Hashimoto, T., et al. 2016, *ApJ*, 833, 190
- Tristram, K. R. W., Burtscher, L., Jaffe, W., et al. 2014, *A&A*, 563, A82
- Tully, R. B., Rizzi, L., Shaya, E. J., et al. 2009, *AJ*, 138, 323
- Veilleux & Osterbrock 1987.
- Veilleux, S., Shopbell, P. L., & Miller, S. T. 2001, *AJ*, 121, 198
- Wada, K. 2012, *ApJ*, 758, 66
- Wada, K. 2015, *ApJ*, 812, 82
- Wada, K., Schartmann, M., & Meijerink, R. 2016, *ApJL*, 828, L19
- Wada, K., Fukushige, R., Izumi, T., & Tomisaka, K. 2018, *ApJ*, 852, 88
- Wilson, A. S., Shopbell, P. L., Simpson, C., et al. 2000, *AJ*, 120, 1325
- Zhang, Z. T., Liang, Y. C., & Hammer, F. 2013, *MNRAS*, 430, 2605